Tilt Phenomenon in Bistatic SAR Image

Viet T. Vu, *Senior Member, IEEE*, and Mats I. Pettersson, *Senior Member, IEEE*

***Abstract*— The tilt phenomenon or skew in bistatic synthetic aperture radar (SAR) images has been known. This can be observed from the SAR image of a point-like scatterer, even with a symmetrical bistatic aperture. This letter explains this phenomenon in bistatic SAR images and shows that the phenomenon depends on the initial and the last positions of the transmitter and receiver platforms. A formula to calculate the tilt angle based on a general bistatic geometry is provided. This formula supports bistatic SAR system design and bistatic image quality measurements.**

***Index Terms*— Bistatic, synthetic aperture radar (SAR), skew, tilt, ultrawidebeam (UWB).**

I. Introduction

SAR is a radar technique synthesizing a large aperture based on the movement of the radar platform. The synthesized aperture is therefore much larger than the physical radar aperture. This radar technique has been used for a wide range of applications such as imaging, change detection, and ground moving target indication (GMTI). Bistatic synthetic aperture radar (SAR) has been attracting great interest thanks to the advantages over monostatic SAR such as reducing vulnerability, avoiding radar jamming, and deception, and enhancing the classification capability.

The research on bistatic SAR was started with the emergence of the bistatic experiments with different combinations of airborne and spaceborne [1], [2]. The practical issues in the bistatic SAR experiments such as synchronization and calibration have been appropriately investigated, whereas bistatic SAR signal processing has remained an active research area. The diversity of bistatic SAR geometry due to the diversity of platform velocity and platform altitude leads to known and unknown issues in bistatic SAR signal processing. A typical known issue is the sum of two square roots coming from the sum of ranges from transmitter and receiver, preventing an exact solution of the stationary point that requires to derive the 2-D Fourier transform of a bistatic SAR signal matrix [3]. Another issue is bistatic SAR resolution that has been investigated and reported in [4] and [5]. In this letter, we discuss another issue, namely, the tilt phenomenon in bistatic SAR images.

The tilt phenomenon or skew can be observed in monostatic SAR images with a squinted line of sight as shown in [6]. The same effect is observed in bistatic SAR images of a point-like scatterer [3]. This phenomenon is believed to depend on the motion parameters of the transmitter and receiver platforms. However, there has been no further investigation about this issue although it is important for bistatic SAR system design and bistatic image quality measurements.

In this study, we investigate the tilt phenomenon in bistatic SAR images. The investigations show that the tilt angle depends on the initial and the last positions of the transmitter and receiver platforms or flight paths. The tilt phenomenon strongly affects the spatial resolutions of a bistatic SAR system. An analytical calculation of the tilt angle based on a bistatic geometry is provided in this study. With a suitable selection of flight paths for a bistatic SAR system, this phenomenon can be avoided.

The rest of this letter is organized as follows: the bistatic ω–k relationship, that is fundamental to understanding the tilt phenomenon, is presented in Section II. In Section III, we investigate the tilt phenomenon and propose the formula to calculate the tilt angle. Section IV provides the simulations to verify the proposed formula. Further discussions about bistatic SAR area resolution and image quality assessments are given in Section V. Section IV presents some conclusions.

II. Bistatic ω–k Relationship

An $\omega - k$ relationship for bistatic SAR is a function of radar signal frequency, Doppler frequency, and bistatic geometry. The bistatic geometry is represented by the bistatic factor χ. As proposed in [5], a general ω–k relationship for bistatic SAR is given by

$$\omega = \frac{c}{2\chi}\sqrt{k_\xi^2 + k_\rho^2} \tag{1}$$

where $\omega = 2\pi\nu$ is the angular frequency

$$k_\xi = \frac{2\pi\nu}{c}(\sin\alpha_T + \sin\alpha_R) = \frac{4\pi\nu}{c}\chi_\xi \tag{2}$$

and

$$k_\rho = \frac{2\pi\nu}{c}\left(\cos\alpha_T\frac{\cos\beta_T}{\cos\beta} + \cos\alpha_R\frac{\cos\beta_R}{\cos\beta}\right) = \frac{4\pi\nu}{c}\chi_\rho. \tag{3}$$

The angles in (2) and (3) are defined in Fig. 1, in which $\alpha_{(\cdot)}$ are the angles formed by $\vec{r}_{(\cdot)}$ and $\vec{\rho}_0$, $\beta_{(\cdot)}$ are the angles formed by $\vec{r}_{(\cdot)}$ and the ground plane, and β is the angle formed by $\vec{r}$ and the ground plane. Herein, we assume a flat surface and a rectilinear geometry of the transmitter and receiver with respect to the ground.

The angles $\alpha_{(\cdot)}$ and $\beta_{(\cdot)}$ change with respect to the positions of the transmitter and receiver during the measurement time and define χ_ξ and χ_ρ. Hence, the bistatic factor χ, χ_ξ defined in (2) and χ_ρ defined in (3) are functions of azimuth time and related by

$$\chi(t) = \sqrt{\chi_\xi^2(t) + \chi_\rho^2(t)}. \tag{4}$$

Manuscript received September 27, 2021; revised November 15, 2021 and December 22, 2021; accepted January 6, 2022. Date of publication January 11, 2022; date of current version January 25, 2022. *(Corresponding author: Viet T. Vu.)*

The authors are with the Blekinge Institute of Technology, 37179 Karlskrona, Sweden (e-mail: viet.thuy.vu@bth.se).

Digital Object Identifier 10.1109/LGRS.2022.3141845

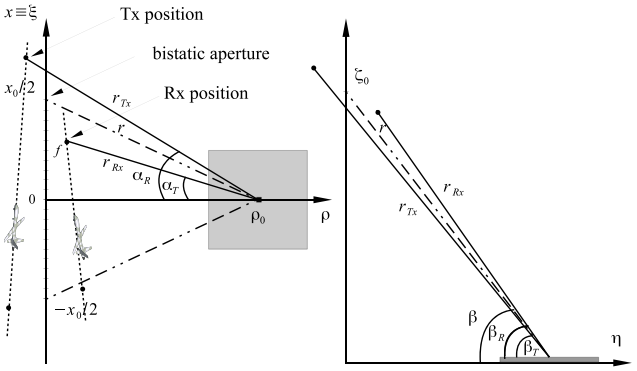

Fig. 1. Bistatic SAR geometry.

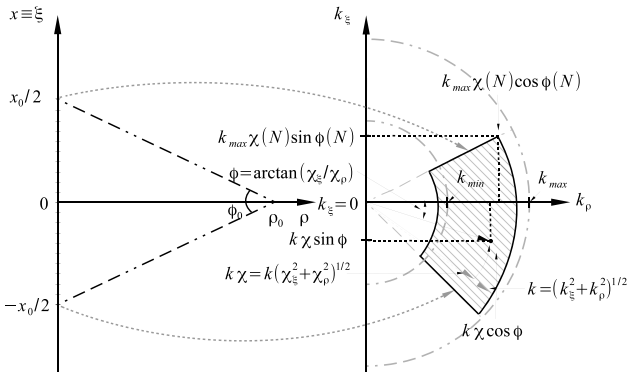

Fig. 2. Bistatic SAR region of support.

For simplicity, we write only χ, χ_ξ and χ_ρ without the variable t. In terms of trigonometry, χ is a function of the arch but the arch border cannot be expressed analytically due to the complex variation of χ.

Fig. 2 shows an illustration on the region of support for a general bistatic case. A point in the bistatic region of support given by $(k\chi \sin\phi, k\chi \cos\phi)$ corresponds to a point in the wavenumber plane (k_ξ, k_ρ) and defined by the vector magnitude

$$k\chi = \frac{2\omega\chi}{c} = \sqrt{k_\xi^2 + k_\rho^2} \tag{5}$$

and the vector direction

$$\phi = \arctan\left(\chi_\xi/\chi_\rho\right). \tag{6}$$

The maximum and minimum values of k are defined by the maximum and minimum frequencies, respectively, i.e., $k_{\min} = 4\pi\nu_{\min}/c$ and $k_{\max} = 4\pi\nu_{\max}/c$. Without the bistatic factor χ, (5) is the equation for the Stolt mapping from the ω to the wavenumber domain [7], [8], part of the ω–k processing algorithm. Hence, (5) is seen to be the modified form of the Stolt mapping for the bistatic cases.

III. Investigations Based on ω–k Relationship

Consider a bistatic SAR system synthesizing an aperture with the measurements from the first position to the Nth position (the last position). The data are used to form an SAR image. The 2-D Fourier transform of the image is illustrated on the right-hand side of Fig. 2. As observed, the left and right borders of the bistatic region of support will be defined by $k_{\min}\chi$ and $k_{\max}\chi$, respectively. However, the lower border of the bistatic region of support will refer to the initial bistatic aperture position $[x(1), y(1), z(1)]$ and therefore defined by a line going through two points

$$(k_{\min}\chi(1)\cos\phi(1), k_{\min}\chi(1)\sin\phi(1))$$
$$(k_{\max}\chi(1)\cos\phi(1), k_{\max}\chi(1)\sin\phi(1))$$

where $\phi(1) = \arctan(\chi_\xi(1)/\chi_\rho(1))$.

Similarly, the upper border of the bistatic region of support will refer to the last bistatic aperture position $[x(N), y(N), z(N)]$ and correspondingly defined by a line going through two points

$$(k_{\min}\chi(N)\cos\phi(N), k_{\min}\chi(N)\sin\phi(N))$$
$$(k_{\max}\chi(N)\cos\phi(N), k_{\max}\chi(N)\sin\phi(N))$$

where $\phi(N) = \arctan(\chi_\xi(N)/\chi_\rho(N))$.

It is worth mentioning that the aperture position n that corresponds to the azimuth wavenumber $k_\xi(n) = 0$ must fulfill the condition

$$k_\xi(n) = \frac{2\pi\nu}{c}\chi_\xi(n) = 0 \tag{7}$$

or

$$\chi_\xi(n) = \sin\alpha_T(n) + \sin\alpha_R(n) = 0 \tag{8}$$

and generally, $n \neq N/2$.

The geometrical integration angle is estimated by the initial and the last bistatic aperture positions and the minimum range. For a symmetrical geometry shown on the left-hand side of Fig. 2, it can be easily estimated by $\phi_0 = 2\arctan(x_0/2\rho_0)$. However, the practical integration angle or the bistatic integration angle will be estimated by the angle formed by the lower and upper borders of the bistatic region of support

$$\phi_p = |\phi(1)| + |\phi(N)| = \left|\arctan\frac{\chi_\xi(1)}{\chi_\rho(1)}\right| + \left|\arctan\frac{\chi_\xi(N)}{\chi_\rho(N)}\right|. \tag{9}$$

Hence, the bistatic integration angle is generally different from the geometrical integration angle, i.e., $\phi_p \neq \phi_0$.

In the case, $|\phi(1)| \neq |\phi(N)|$, the region of support is tilted by an angle

$$\Delta\phi = \frac{1}{2}\Big||\phi(1)| - |\phi(N)|\Big|. \tag{10}$$

The bistatic SAR image is therefore supposed to be tilted by the same angle. The tilt phenomenon results in the degradation of the area resolution and the spatial resolutions as consequence. In addition, the tilt phenomenon also leads to certain difficulties in evaluating bistatic SAR system performance. The degradation of resolution will be discussed in Section V-A and the image quality assessments will be discussed in Section V-B.

To avoid this tilt, the initial and the last positions of the platforms must satisfy the condition $|\phi(1)| = |\phi(N)|$ or in other words

$$\left|\frac{\chi_\xi(1)}{\chi_\rho(1)}\right| = \left|\frac{\chi_\xi(N)}{\chi_\rho(N)}\right| \tag{11}$$

TABLE I
SIMULATION PARAMETERS

Parameter	Transmitter	Receiver
Maximum frequency	82.5 MHz	
Minimum frequency	22.0 MHz	
Platform speed v_{pl}	129 m/s	43 m/s
Aperture step	0.9375 m	0.3125 m
Flight altitude	3700 m	2000 m
PRF	137 Hz	
Num. aperture position	20480	
Case 1		
Initial coordinates	$(-3444, -721)$	$(-9319, 721)$
Last coordinates	$(15737, -1558)$	$(-2975, 1558)$
Flight headings	-2.5^{o}	7.5^{o}
Case 2		
Initial coordinates	$(-9344, -721)$	$(-3419, 721)$
Last coordinates	$(9837, -1558)$	$(2956, 1558)$
Flight headings	-2.5^{o}	7.5^{o}

where χ_ξ and χ_ρ are defined in (2) and (3), respectively, and calculated easily from the initial and the last positions of the platforms.

IV. VERIFICATION

The aim of this section is to verify (10), (11) by the simulations. We consider two cases: $|\phi(1)| \neq |\phi(N)|$ and $|\phi(1) \approx \phi(N)|$. Both the cases are simulated with symmetrical bistatic apertures. The tilt angles $\Delta\phi$ resulted by the simulations are measured on the bistatic SAR images formed with the simulated data and then compared to the values given by (10) and (11), i.e., theoretical values. If the measured values and theoretical values are identical, (10) and (11) will be said to be verified.

A. Arrangement

The parameters of the Coherent All-Radio Band Sensor-II system (CARABAS-II) and CARABAS-III are considered for the simulations [9], [10]. The passive receiver is simulated with the motion parameters of CARABAS-III (speed and altitude of a helicopter), whereas the transmitter is simulated with the radar and motion parameters of CARABAS-II (speed and altitude of an aircraft). The main parameters for the simulations are summarized in the first part of Table I. Some supplemental parameters for the simulations of the two considered cases are given in the second and third parts of the table.

With the given radar parameters, the fractional bandwidth is estimated by $B/f_c \approx 1.2$. With 20480 aperture positions with an aperture step of 0.9375 m, the geometrical integration angle is up to $\phi_0 \approx 103.5°$. The considered parameters allow us to simulate an ultrawideband ultrawidebeam (UWB) SAR system. The motion parameters of a helicopter are much different from those of an aircarft. Specifically, in the simulations, the speed of the receiver platform (helicopter) is 3 times lower than that of the transmitter platform (aircraft), whereas the difference between the flight altitudes of the platforms is about 1700 m. It is obvious that we can obtain extreme bistatic geometries with these motion parameters. Hence, the parameters used for the simulation are supposed to be comprehensive enough to verify the tilt phenomenon. However, we need to assume that the antennas are omni-directional and the spatial synchronization is managed successfully.

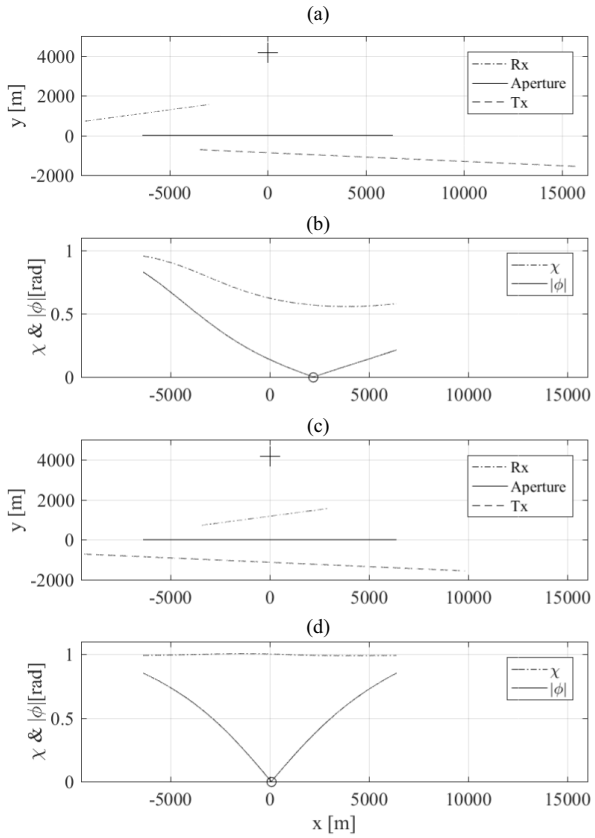

Fig. 3. Simulated SAR geometries for different cases and different bistatic factors. (a) Case 1-bistatic geometry. (b) Case 1-bistatic factors. (c) Case 2-bistatic geometry. (d) Case 2-bistatic factors.

The ground scene is simulated with a single point-like scatterer placed in the center of the SAR scene. It is marked by the cross in the upper part of Fig. 3(a) and (c). The radar cross section (RCS) of the scatterer is normalized to one.

For Case 1, the flight headings and initial coordinates are given in the second part of Table I. The flight paths of the platforms are plotted in Fig. 3(a). The midpoints of the transmitter and receiver flight paths define the bistatic aperture that is marked by the black solid line in the same plot. The bistatic aperture is shown to be symmetrical with respect to the point-like scatterer.

For Case 2, we regulate the initial positions in the x-direction of the transmitter and receiver platforms by shifting the initial positions of the transmitter to the right-hand side and that of the receiver platform to the left-hand side. Other parameters of Case 1 are maintained. The initial coordinates are provided in the third part of Table I. The flight paths of transmitter and receiver platforms are plotted in Fig. 3(c). The bistatic aperture is shown to be symmetrical with respect to the point-like scatterer.

B. Case 1: $|\phi(1)| \neq |\phi(N)|$

With the known coordinates of the transmitter and receiver platforms as shown in Fig. 3(a), the values of χ and ϕ can

be retrieved by (4) and (6), respectively. These values are plotted in Fig. 3(b) as a function of the bistatic aperture. The bistatic factors χ and ϕ complicatedly vary. For χ, the varying range is found in the range [0.5805, 0.9562]. The varying of ϕ is found in the range [−0.8297 rad, 0.2136 rad] or [−47.54°, 12.24°]. The lower bound of the angle ϕ is given by the angle associated with the initial positions of the transmitter and receiver, i.e., $\phi(1) = -47.54°$. The last positions of the transmitter and receiver determine the upper bound of the angle ϕ, i.e., $\phi(N) = 12.24°$. The practical integration angle in this case is estimated with (9) and equal to $\phi_p \approx 59.78°$. Compared with the geometrical integration angle ϕ_0, we can see that the practical integration angle is only about half of the geometrical integration angle. Using (10), we can find the tilt angle of $\Delta\phi = 17.65°$.

Fig. 4(a) shows the zoomed-in part of the SAR image formed in the slant-range plane (ξ, ρ) with the global back-projection algorithm for bistatic SAR presented in [11]. The simulated point-like scatterer is well focused in the SAR image, and we can observe the effects of both the UWB and bistatic characteristics from sidelobes of the point-like scatterer.

A narrowband narrowbeam region of support can be approximated by a rectangular area, the 2-D inverse Fourier transform of the rectangular area results in a 2-D sinc function. The sidelobes are in only range and cross-range. For the UWB systems, the rectangular approximation is invalid. The 2-D inverse Fourier transform of an arc results in a point target with complex sidelobes spreading in different directions in the SAR image.

The SAR image is tilted by an angle that is estimated by (9). The tilt axis is plotted in the same figure by the solid gray line for illustrating the tilt angle. The axis goes through the main lobe and two peak sidelobes on the opposite sides of the main lobe. The measurement gives a tilt angle of $\Delta\phi = 18.43°$ that is similar to the $\Delta\phi$ estimated with (10).

The 2-D Fourier transform of the SAR image giving the region of support is provided in Fig. 4(b) in the form of arch. The angles $\phi(1)$, $\phi(N)$ and the bistatic integration angle measured on the region of support are similar to the values given by (6) and (9).

C. Case 2: $|\phi(1)| \approx |\phi(N)|$

Consider the flight paths of the transmitter and receiver platforms given in Fig. 3(c). The values of χ and ϕ calculated with (4) and (6), respectively, are plotted in Fig. 3(d). The bistatic factor χ varies slightly in the range [0.9878, 1.0033] while the other bistatic factor ϕ is in the range [−0.8509 rad, 0.8509 rad] or [−48.75°, 48.76°]. In this case, $|\phi(1)| \approx |\phi(N)| = 48.75°$ and the practical integration angle is $\phi_p \approx 2|\phi(1)| = 97.51°$. Compared with the geometrical integration angle ϕ_0, we can see that the practical integration is still smaller than the geometrical integration angle. However, compared with the practical integration angle in Case 1, we can see that a much larger practical integration angle is obtained. The tilt angle in this case will approximately be zero $\Delta\phi \approx 0°$.

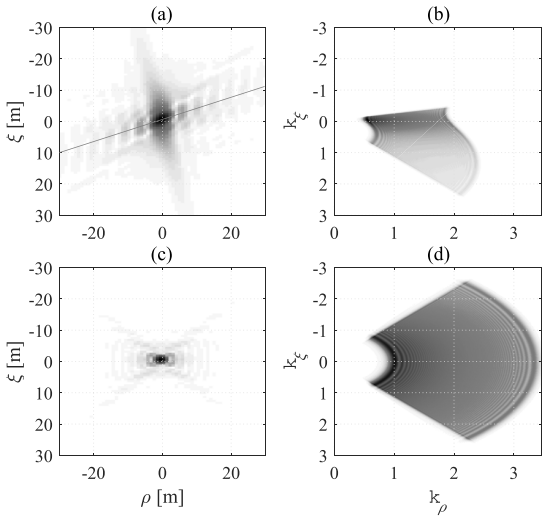

Fig. 4. SAR images and regions of support in cases. (a) Case 1: SAR image. (b) Case 1: region of support. (c) Case 2: SAR image. (d) Case 2: region of support.

Fig. 4(c) provides the zoomed-in part of the SAR image in the slant-range plane (ξ, ρ). The simulated point-like scatterer is also well focused and looks like the SAR image in the monostatic case. We can only observe the effects of the UWB characteristics but not the effects of bistatic characteristics, i.e., there is no tilt. Comparing Fig. 4(c) to (a), we can see a significant improvement in the area resolution.

The 2-D inverse Fourier transform of the SAR image giving the region of support is provided in Fig. 4(d) in the form of a symmetrical arch and is similar to the region of support in the monostatic case. Comparing Fig. 4(d) to (b), we can see that a much larger region of support is achieved.

V. Further Discussions

The considered cases in Section IV show that the selection for the flight paths of the transmitter and receiver platforms is important for the efficiency of a bistatic SAR system. It also simplifies the assessments for a bistatic SAR system as discussed in this section.

A. Bistatic SAR Area Resolution

According to Table I, the difference between Case 1 and Case 2 is only the initial position of the transmitter and receiver platforms in the x-direction, whereas the number of aperture positions, the velocities of the platforms, the flight altitudes, and even the positions in y-direction are identical. However, the retrieved regions of support and the practical integration angles in two cases are totally different. For Case 1, the motion parameters of the platform result in a very small region of support. Consequently, the corresponding value of area resolution is large (low resolution) since the limit of area resolution ΔA is inversely proportional to the region of support Ω [5]

$$\Delta A \geq (2\pi)^2 \times \Omega^{-1}. \tag{12}$$

For Case 2, a significantly larger region of support is obtained, and the value of area resolution is therefore small (high resolution). Hence, a selection of bistatic geometry has

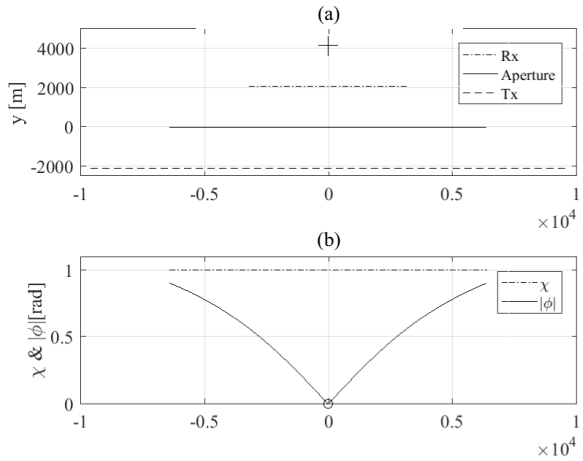

Fig. 5. Bistatic SAR geometry with $\chi = 1$ and $\tilde{\phi}_0 = \phi_0$. (a) Special case-bistatic geometry. (b) Special case-bistatic factors.

a significant influence on the area resolution achieved by the SAR system.

The investigations in Section II show that, the right and left borders of the regions of support are determined by the bistatic factor χ while bistatic factor ϕ decides the lower and upper borders. In addition, the bistatic factors χ and ϕ are dependent and linked together by (4) and (6). To maximize the region of support, the values χ, $\phi(1)$ and $\phi(N)$ should be maximum. The values $\phi(1)$ and $\phi(N)$ reach maximum when $\chi_\xi(1)$ and $\chi_\xi(N)$ reach maximum and are derived from (2) by

$$\chi_\xi = \sin\left(\frac{\alpha_T + \alpha_R}{2}\right)\cos\left(\frac{\alpha_T - \alpha_R}{2}\right) \le \sin\alpha. \tag{13}$$

The equal sign of (13) occurs when $\alpha = \alpha_T = \alpha_R$. In addition, the maximum practical integration angle is obtained with the symmetrical geometries of the transmitter and receiver platforms, i.e., $|\alpha(1)| = |\alpha(N)|$. If we only consider (13), the larger the separation between transmitter and receiver platforms is, the larger the angle $\sin\alpha$ is, or in other words, the wider practical integration angle ϕ_p we obtain.

For the considered case where $\alpha = \alpha_T = \alpha_R$, χ_ρ is simplified to

$$\chi_\rho = \frac{\cos\alpha}{\cos\beta}\cos\left(\frac{\beta_T + \beta_R}{2}\right)\cos\left(\frac{\beta_T - \beta_R}{2}\right) \approx \cos\alpha\cos\Delta\beta. \tag{14}$$

The bistatic factors are given and limited by

$$\chi = \sqrt{\sin^2\alpha + \cos^2\alpha\cos^2\Delta\beta} \le 1 \tag{15}$$

$$\phi_p = 2\left|\arctan\left(\frac{\tan\alpha(1)}{\cos\Delta\beta(1)}\right)\right| \le 2|\alpha(1)|. \tag{16}$$

The equal signs in (15) and (16) occur when $\beta_T = \beta_R$. Fig. 5 shows an example of bistatic SAR geometry and bistatic factors in this case.

B. Image Quality Assessments

With the arrangement in Case 1, the bistatic SAR image is tilted with an angle given by (9). The currently used image quality assessments for monostatic SAR such as spatial resolutions, peak sidelobe ratio, and integrated sidelobe ratio need to be modified for the bistatic case. For example, the range resolution should be measured on the tilt axis instead of the ρ-axis, whereas the azimuth resolution cannot be measured on the ξ-axis. An alternative is to remove the tilt by shearing the image along the range time axis [3]. These issues should be further investigated. However, in Case 2 and the special case considered in Section V-A, the currently used image quality assessments for monostatic SAR can be directly applied without any modification.

VI. Conclusion

This letter presented a discussion about the tilt phenomenon in bistatic SAR images. The results provided in this letter showed that the tilt angle depends on the initial and the last positions of the transmitter and the receiver platforms that define the flight paths of the platforms. The analytical calculation of the tilt angle based on bistatic SAR geometry was derived that supports designing bistatic SAR systems. The simulation results based on the CARABAS parameters verified the relevant derived equations. Further discussions on bistatic SAR area resolution and image quality assessments were also provided to show the importance of the selection of the flight paths of the transmitter and receiver platforms. Although the reference system for this study is a UWB system, the results can be used for narrowband narrowbeam systems such as spaceborne SAR systems.

References

[1] I. Walterscheid *et al.*, "Bistatic SAR experiments with PAMIR and TerraSAR-X—Setup, processing, and image results," *IEEE Trans. Geosci. Remote Sens.*, vol. 48, no. 8, pp. 3268–3279, Aug. 2010.

[2] R. Baque *et al.*, "LORAMbis a bistatic VHF/UHF SAR experiment for FOPEN," in *Proc. IEEE Radar Conf.*, Washington, DC, USA, May 2010, pp. 832–837.

[3] Y. L. Neo, F. Wong, and I. G. Cumming, "A two-dimensional spectrum for bistatic SAR processing using series reversion," *IEEE Geosci. Remote Sens. Lett.*, vol. 4, no. 1, pp. 93–96, Jan. 2007.

[4] W. Dower and M. Yeary, "Bistatic SAR: Forecasting spatial resolution," *IEEE Trans. Aerosp. Electron. Syst.*, vol. 55, no. 4, pp. 1584–1595, Aug. 2019.

[5] V. T. Vu, "Area resolution for bistatic ultrawideband ultrawide-beam SAR," *IEEE Trans. Aerosp. Electron. Syst.*, vol. 57, no. 2, pp. 1371–1377, Apr. 2021.

[6] G. W. Davidson and I. Cumming, "Signal properties of spaceborne squint-mode SAR," *IEEE Trans. Geosci. Remote Sens.*, vol. 35, no. 3, pp. 611–617, May 1997.

[7] R. H. Stolt, "Migration by Fourier transform," *Geophysics*, vol. 43, no. 1, pp. 23–48, 1978.

[8] C. Cafforio, C. Prati, and F. Rocca, "Full resolution focusing of seasat SAR images in the frequency-wave number domain," *Int. J. Remote Sens.*, vol. 12, no. 3, pp. 491–510, Mar. 1991.

[9] A. Gustavsson *et al.*, "Development and operation of an airborne VHF SAR system-lessons learned," in *Proc. IEEE IGARSS*, vol. 1, Seattle, WA, USA, Jul. 1998, pp. 458–462.

[10] H. Hellsten, S. Sahlin, and P. Dammert, "Polarimetric subsurface SAR imaging outcome of theoretical development and CARABAS III tests," in *Proc. Int. Radar Conf.*, Lille, France, Oct. 2014, pp. 1–8.

[11] V. T. Vu, T. K. Sjogren, and M. I. Pettersson, "Fast time-domain algorithms for UWB bistatic SAR processing," *IEEE Trans. Aerosp. Electron. Syst.*, vol. 49, no. 3, pp. 1982–1994, Jul. 2013.